

Article

A Study of Physical Modeling and Mathematical Modeling on Inclusion Behavior in a Planar Flow Casting Process

Yu Liu ^{*}, Hao Qiu, Zixu He, Yue Yu and Heping Liu ^{*}

Central Iron and Steel Research Institute, Beijing 100081, China; qiuhaogangyan@163.com (H.Q.); yuliu2@kth.se (Z.H.); 18622164233@163.com (Y.Y.)

* Correspondence: liuyu_901008@163.com (Y.L.); liuhp07@163.com (H.L.); Tel.: +86-18811794336 (H.L.)

Abstract: Flow pattern and inclusion removal in a novel-designed crucible in the planar flow casting process were studied in the present paper. A color dye water experiment was used to show the flow field and validate the mathematical modeling. It was shown that the flow pattern predicted by the Large Eddy Simulation model is maximally consistent with that in the physical modeling. The validated mathematical model was used to predict the flow pattern and inclusion behavior in the crucible with various prototypes using combinations of multiple facilities. The results show that the flow field, by using the stopper, enhances compared to that using none of the facilities, which causes the inclusion removal to become even worse when the stopper is individually used. Furthermore, as the magnetic field is added, the electromagnetic brake weakens the flow field in the magnetic zone. The function of the electromagnetic brake to weaken the flow pattern is most efficient for inclusion removal.

Keywords: planar flow casting process; physical and mathematical modeling; inclusion removal; FeSiB amorphous alloy



Citation: Liu, Y.; Qiu, H.; He, Z.; Yu, Y.; Liu, H. A Study of Physical Modeling and Mathematical Modeling on Inclusion Behavior in a Planar Flow Casting Process. *Metals* **2022**, *12*, 606. <https://doi.org/10.3390/met12040606>

Academic Editors: Menachem Bamberger and Nikki Stanford

Received: 27 October 2021

Accepted: 28 March 2022

Published: 31 March 2022

Publisher's Note: MDPI stays neutral with regard to jurisdictional claims in published maps and institutional affiliations.



Copyright: © 2022 by the authors. Licensee MDPI, Basel, Switzerland. This article is an open access article distributed under the terms and conditions of the Creative Commons Attribution (CC BY) license (<https://creativecommons.org/licenses/by/4.0/>).

1. Introduction

The amorphous material has several unique properties, such as incredible magnetism, excellent corrosion resistance, high resistivity, and high electromechanical coupling coefficient, because of its components and disordered structure. Due to its outstanding properties, the amorphous material can be used to manufacture electromagnetic equipment [1–3]. The planar flow casting (PFC) process is most often used to produce the amorphous ribbon. The refined master alloy is poured into tundish for inclusion removal and thermal preservation in the PFC process. After that, the melt flows into a crucible through a submerged nozzle. The molten alloy passes through a slit nozzle at the bottom of the crucible and is sprayed on a copper cooling roller to produce the amorphous ribbon. The rotational speed of the copper roller varies in the range of 15 m/s to 35 m/s, and the cooling rate is approximately 10^6 °C/s [1–3]. The function of cooling water inside the rotating copper roller is to obtain the high cooling rate on the roller surface to promote the formation of the amorphous ribbon and reduce the roller deformation. The width of the slit nozzle is 0.2–1 mm, and the thickness of solidified ribbon is around 30 μm [1,2]. The solid ribbon is thrown out along with the tangent direction of the copper roller surface. Because of the rapid solidification and precision in the PFC process, the atmosphere and process parameters, such as roller rotating velocity and nozzle-roller distance, should be strictly controlled to ensure the surface quality of products [4–6]. The overview of the traditional PFC process is shown in Figure 1 [7].

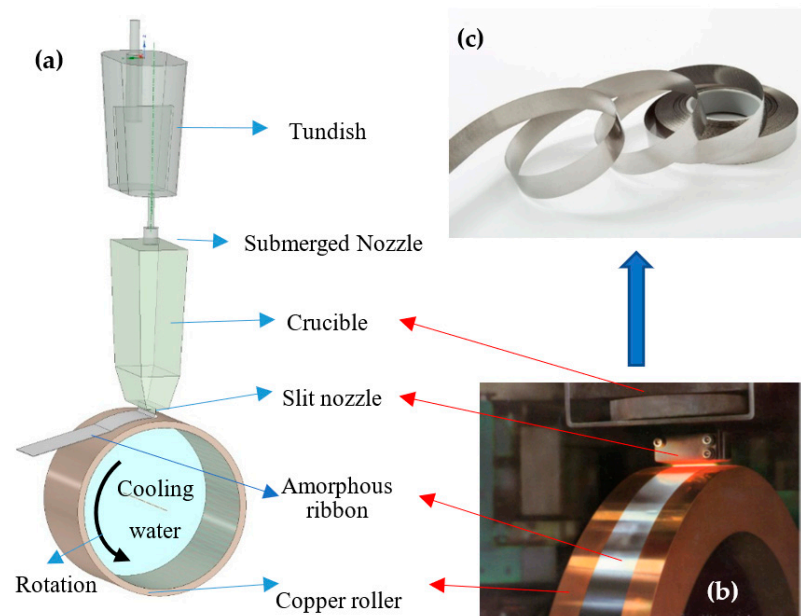


Figure 1. Overview of the PFC process. (a) Schematic diagram, (b) real process diagram, (c) amorphous ribbon. (Figure 1b is reproduced from [7]).

To guarantee the quality of the amorphous ribbon, several aspects should be taken into consideration as follows:

1. Inclusions in the molten master alloy. In the manufacturing process, the inclusion particles in the molten alloy can collide into nodules on the inner wall during a long casting cycle, especially at the nozzle slit with the width of 0.2–1 mm, which could form scratches or defects on the amorphous ribbon and decrease the corrosion resistance performance, even causing serious nozzle slit clogging, interrupting production [8–11].
2. The homogenization of flow field and melt temperature in the long-term and continuous production process. The superheat of melt affects the ribbon's quality and production to a large extent [8–11]. Excessively high superheat could lower the cooling rate, in which case, the amorphous structure would not form. On the contrary, the low melt temperature could lead to an abnormal temperature gradient of melt in the nozzle slit and the puddle [1,12,13].
3. Applying Lorenz force to control the flow and inclusions behavior. It has been reported that an electromagnetic braking field can be employed to adjust the melt flow, temperature distribution, inclusion floating, and solidification, improving the product quality by enhancing the stability and continuity in the continuous casting process [14–17].

In the process to manufacture a broad amorphous ribbon, the crucible and nozzle slit is connected to keep the liquid height and guarantee the outflow at a certain speed, as shown in Figure 1. Compared with the ladle-tundish-continuous casting processes in the traditional steel-making field, the mass flow rate of the melt in PFC process through the slit nozzle is far less than that of the molten steel into the mold in continuous casting of steel process. The crucible in the PFC process should be specially design for the effective control of the flow and inclusion behaviors of the melt. In order to manufacture the amorphous ribbon with uniform thickness and excellent qualities, there exist several following issues in this process: firstly, when the molten liquid gravitationally flows from the tundish into the crucible, it is possible to cause a severe disturbance, so the oxidation layer at the top interface could be trapped into molten steel and form the oxide inclusions. Secondly, in terms of various nozzle slits' designs, the non-uniform flow in the crucible could lead to horizontal unevenness of the thickness on the ribbon surface. Finally, during long-term

manufacturing, the fluctuation of liquid height is one of the main problems influencing the uniform flow and temperature distribution, which directly determine the ribbon's quality, especially at the beginning and final [12,13,17].

Several studies on the planar flow casting process using mathematical modeling [17–25] have been reviewed. The effects of flow pattern, puddle shape, and wetting conditions on the surface quality of the amorphous ribbon are studied extensively. Moreover, a few studies [25–29] on the temperature distribution in the puddle and copper roller and the thermal deformation of copper roller were also carried out. However, few works on the inclusion behavior in the crucible using mathematical modeling have been carried out. Therefore, through physical and mathematical modeling, the research objective of the present work is to improve flow stability, temperature homogenization, and reduce inclusions. Furthermore, a new facility designed with continuous tundish-crucible and electromagnetic field are innovatively proposed for the broad ribbon production. Furthermore, the flow pattern and inclusion behavior in the crucible have been studied using physical and mathematical modeling.

2. Model Description

Regarding mathematical modeling, the calculation domain and mesh were shown in Figure 2. The geometry of the crucible was designed by considering the adaption to the structure of the slit nozzle and the requirement for the ejection pressure by establishing the melt level. The **Volume of Fluid (VOF)** model was used to predict the multiphase behaviors in the crucible. The function of the porous baffle was added using the **Porous Media** model. The **Species Transport Model** was used to model the tracer behavior along with the time. The **Discrete Phase Model (DPM)** was employed to predict the behavior of inclusion particles with various sizes. Moreover, the **Magnetohydrodynamics (MHD)** model was used to give the Lorentz force on the melt for the electromagnetic brake [30].

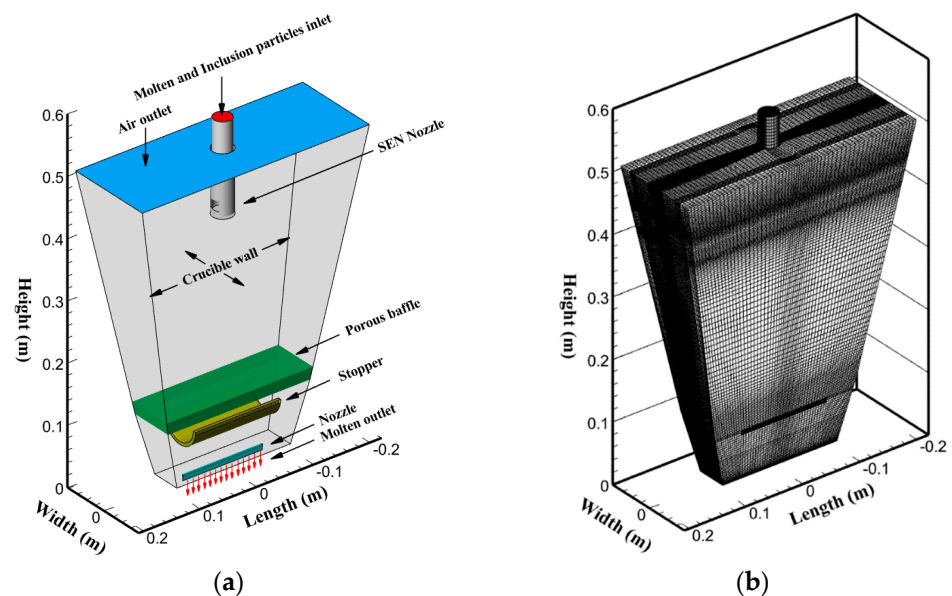


Figure 2. Calculation domain and mesh. (a) Domain; (b) Mesh.

Continuity Equation:

$$\frac{\partial \rho}{\partial t} + \nabla \cdot (\rho \vec{u}) = 0 \quad (1)$$

Momentum equation:

$$\frac{\partial}{\partial t} (\gamma \rho \vec{u}) + \nabla \cdot (\gamma \rho \vec{u} \vec{u}) = -\nabla (\gamma p) + \nabla \cdot \left[\gamma (\mu + \mu_t) \left(\nabla \vec{u} + \nabla \vec{u}^T \right) \right] + \gamma \rho \vec{g} + S_q + F_L \quad (2)$$

ρ is the fluid density ($\text{kg}\cdot\text{m}^{-3}$), μ is the liquid viscosity ($\text{kg}\cdot\text{m}^{-1}\cdot\text{s}^{-1}$), γ is the porosity of the baffle, \vec{u} is velocity component of the fluid ($\text{m}\cdot\text{s}^{-1}$), \vec{g} is the acceleration of gravity ($\text{m}\cdot\text{s}^{-2}$), p is static pressure ($\text{N}\cdot\text{m}^{-2}$), μ_t is the turbulent viscosity ($\text{kg}\cdot\text{m}^{-1}\cdot\text{s}^{-1}$), and S_q is the momentum source term added in the porous media zone, where

$$S_q = -\left(\frac{\mu}{a}\mu_r\vec{u} + C_{ir}\frac{1}{2}\rho|\vec{u}|\vec{u}\right) \quad (3)$$

where μ_r is the relative viscosity ($\text{kg}\cdot\text{m}^{-1}\cdot\text{s}^{-1}$), a is the permeability, and C_{ir} is the inertial resistance factor. Moreover, F_L is the electromagnetic force affecting the fluid flow through the external magnetic field.

Volume of Fluid (VOF) model

$$\frac{\partial\alpha}{\partial t} + \vec{u}\cdot\nabla\alpha = 0 \quad (4)$$

The density and viscosity of the mixed fluid in each cell were calculated as follows:

$$\rho = \alpha\rho_l + (1 - \alpha)\rho_g \quad (5)$$

$$\mu = \alpha\mu_l + (1 - \alpha)\mu_g \quad (6)$$

where ρ_l and ρ_g are the liquid and gas density ($\text{kg}\cdot\text{m}^{-3}$), μ_l and μ_g are the liquid and gas viscosity ($\text{kg}\cdot\text{m}^{-1}\cdot\text{s}^{-1}$), and α is the volume fraction of liquid.

Discrete Phase Model (DPM)

In the DPM model, the forces on the inclusion particles were calculated as follows:

$$\frac{d\vec{u}_p}{dt} = \frac{\vec{u} - \vec{u}_p}{\tau_r} + \frac{\vec{g}(\rho_p - \rho)}{\rho_p} + \vec{F}_{drag} \quad (7)$$

$$\tau_r = \frac{\rho_p d_p^2}{18\mu C_D Re} \quad (8)$$

where u_p and ρ_p are the velocity and density of inclusion particles, respectively, τ_r is the inclusion particle relation time, and C_D is the drag coefficient.

Species Transport Model

The mixing condition was predicted by the species transport equation as follows:

$$\frac{\partial}{\partial t}(\rho\varnothing) + \nabla\cdot(\rho\varnothing\vec{u}) = \nabla\cdot(\rho D\nabla\varnothing) \quad (9)$$

where \varnothing is the mass fraction of tracer, and D is the diffusion coefficient of tracer calculated as $D = D_0 + \frac{\mu_{eff}}{\rho Sc_t}$, where D_0 is the laminar diffusion coefficient, μ_{eff} is the efficient viscosity, and Sc_t is turbulent Schmidt number with the default value of 0.7.

Magnetohydrodynamics (MHD) Module

The electromagnetic force F_L was calculated by Lorenz's law:

$$F_L = \vec{J} \times \vec{B} \quad (10)$$

The symbol B is the applied external magnetic field, and J denotes the induced current density.

Moreover, the realizable k-epsilon, k-omega SST, and Large Eddy Simulation (LES) models [30–32] are commonly used to predict the complicated turbulence eddies' phenomenon. In this study, three turbulence models were firstly compared to check the applicability.

The chemical composition of Fe-based amorphous alloy is FeSiB, the density of which is assumed to be 7100 kg/m^3 [23,26,33]. The similarity criterion should be carried out at the

first step, and the volume ratio of the water model and the novel-designed fabrication facility is 1:1. The water model is widely used to research the phenomenon of melt flow [34–36]. The water model experiment combined with numerical simulation is also widely used to study the flow phenomenon in the metallurgical engineering field [37–39]. The physical properties [22,26,33] and operating conditions of the fluids and inclusion particles used in this study (water was only used for model validation) are listed in Table 1. The boundary conditions and initial conditions are listed in Table 2.

Table 1. Physical parameters adopted in the simulation [22,26,33].

Parameter	Value
Water density ($\text{kg}\cdot\text{m}^{-3}$)	998.2
Water viscosity ($\text{Pa}\cdot\text{s}$)	0.001003
Melt density ($\text{kg}\cdot\text{m}^{-3}$)	7100
Melt viscosity ($\text{Pa}\cdot\text{s}$)	0.0042
Melt electrical conductivity ($\text{S}\cdot\text{m}^{-1}$)	8.33×10^6
Melt magnetic permeability ($\text{H}\cdot\text{m}^{-1}$)	1.257×10^{-6}
Air density ($\text{kg}\cdot\text{m}^{-3}$)	1.225
Air viscosity ($\text{Pa}\cdot\text{s}$)	1.894×10^{-5}
Inclusion particle density ($\text{kg}\cdot\text{m}^{-3}$)	2872
Inclusion particle mass flow rate ($\text{kg}\cdot\text{s}^{-1}$)	0.0002

Table 2. Boundary conditions and initial conditions adopted in the simulation.

Boundary Conditions and Initial Conditions	Mass Fraction of Liquid	Mass and Momentum
Molten and inclusion particles inlet	$\alpha = 1$	$\vec{u} = \vec{u}_{in}$
Air outlet	$\alpha = 0$	$P = 0$
SEN Nozzle wall	-	$\vec{u} = 0$
Crucible wall	-	$\vec{u} = 0$
Porous baffle	-	$r = 0.1$
Stopper wall	-	$\vec{u} = 0$
Nozzle wall	-	$\vec{u} = 0$
Molten outlet	$\alpha = 1$	$P = P_{out}$
Molten level	-	$L = 451 \text{ mm}$
Magnetic field	-	$B_y = 0.1 \text{ T}$

In this study, a three-dimension model was established. The solution was carried out using the commercial software ANSYS FLUENT 19.3 [30]. Meshes with grid numbers of approximately 400,000 were used in the simulations. For the solution method, the pressure-based solver was chosen to solve the multiphase formulations explicitly with a Pressure-Implicit with Splitting of Operators (PISO) scheme. The convergence standard is the residual of all the quantities lower than 0.001. The calculations were carried out on a HP Workstation (Palo Alto, CA, USA), using an Intel E5-2680 CPU (Santa Clara, CA, USA) with a frequency of 2.50 GHz. The calculations of flow pattern, mixing condition, and inclusion behavior for each case took approximately one week when using a parallel processing mode.

3. Results and Discussion

3.1. Model Validation

Above all, the color dye experiment was carried out to show the flow field in Figure 3. The flow patterns predicted by realizable k-epsilon, k-omega SST, and LES models were compared with the results in the physical modeling. It was shown that the flow pattern predicted by the LES model is maximally consistent with that in the physical modeling. Additionally, the tracer mixing condition in the mathematical modeling was compared with

that in the physical modeling at various times, as shown in Figure 4. The tracer behavior predicted by mathematical modeling is in good agreement with the color dye motion in the physical modeling at various times during the mixing.

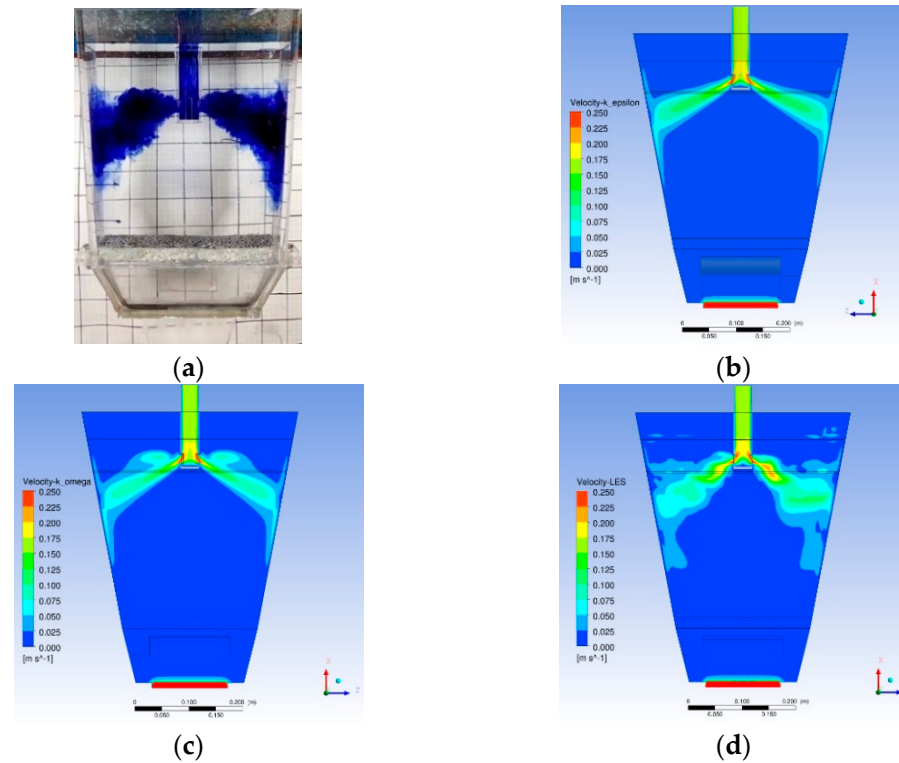


Figure 3. Effect of turbulence model on the predicted flow pattern. (a) Water model experiment, (b) realizable k-epsilon model, (c) k-omega SST model, (d) LES model.

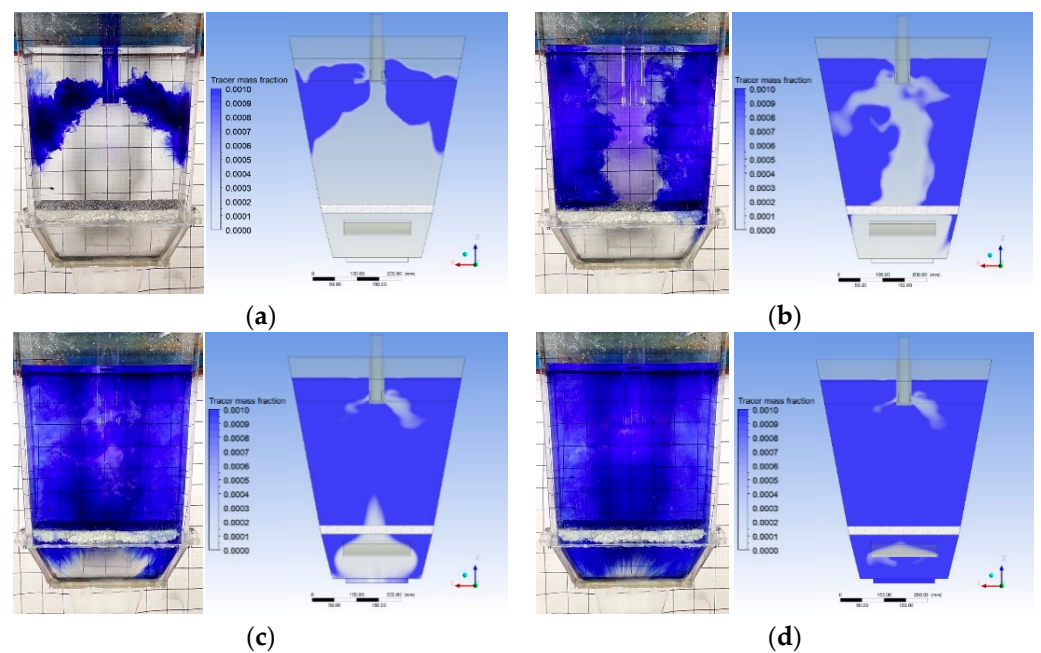


Figure 4. Comparison of tracer behaviors between physical modeling and mathematical modeling. (a) 5 s, (b) 15 s, (c) 25 s, (d) 35 s.

3.2. Flow Field Distribution

Subsequently, the flow patterns using various facilities in the mathematical modeling were shown in Figure 5. Compared to the flow field using none of the facilities in Figure 5a, using the stopper in Figure 5b, the maximum velocity nearby submerged nozzle outlet increases from $0.25 \text{ m}\cdot\text{s}^{-1}$ to around $0.30 \text{ m}\cdot\text{s}^{-1}$. The flow field at the region between the stopper and the slit nozzle enhances obviously. For the flow pattern using stopper and porous baffle in Figure 5c, the velocity nearby the submerged nozzle outflow region decreases to $0.26 \text{ m}\cdot\text{s}^{-1}$, and the flow field becomes intense above the porous zone. Furthermore, when the magnetic field changes due to the direct current as a value of 0.1 tesla is added, the velocity in the central region of the crucible decreases dramatically, as shown in Figure 5d.

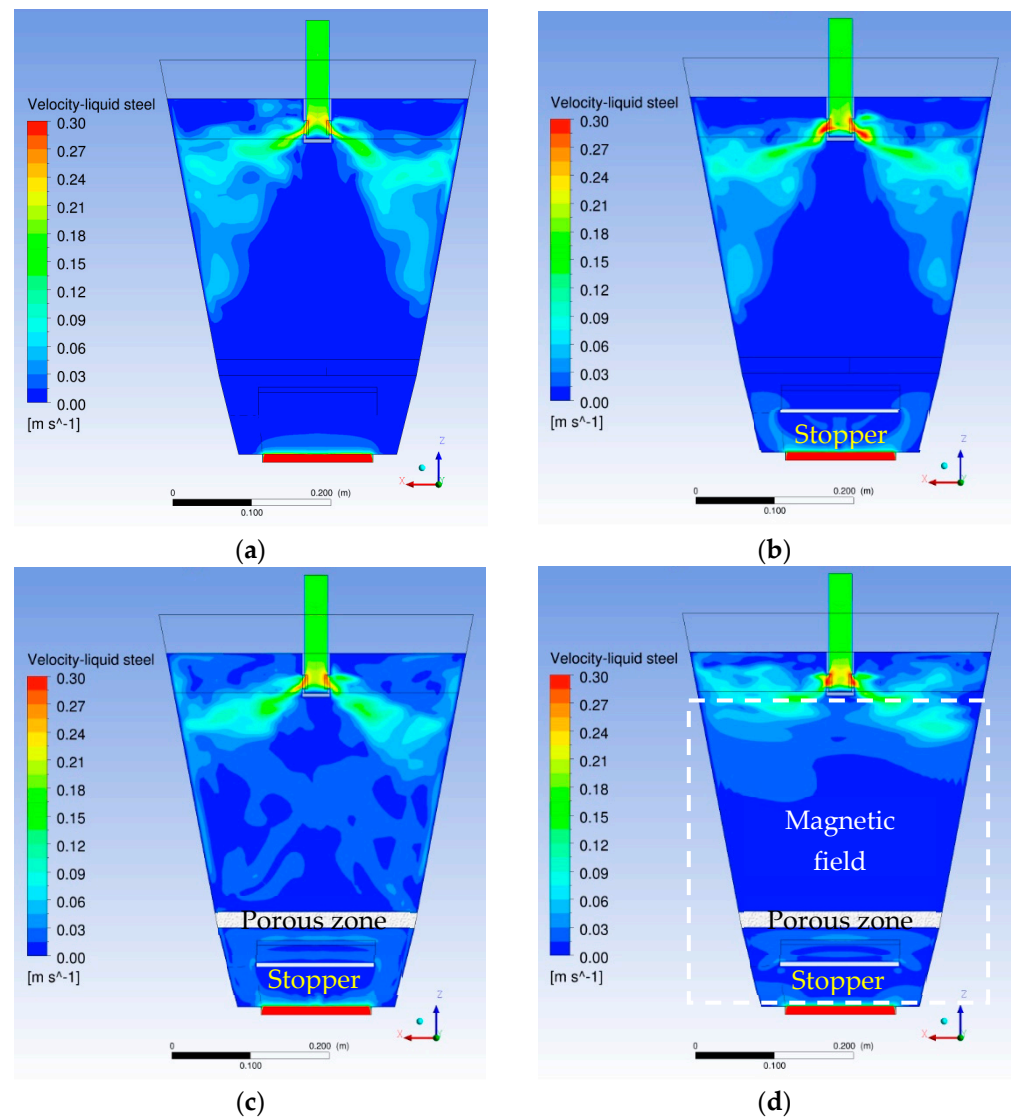


Figure 5. Flow field predicted by the mathematical modeling using various experimental facilities. (a) Without the facilities, (b) with the stopper, (c) with the stopper and porous baffle, (d) with the stopper, porous baffle, and magnetic field.

Near the submerged nozzle outlet, the velocity increases to $0.28 \text{ m}\cdot\text{s}^{-1}$. The function of the electromagnetic brake apparently weakens the flow field in the magnetic zone and enhances the flow circulation above the magnetic zone. Moreover, the flow pattern below the porous zone becomes weaker to a small extent.

3.3. Inclusion Behavior and Removal Ratio

In the mathematical modeling, the behavior of inclusion particles with sizes in the range of 1 μm to 100 μm was studied. The inclusion distribution in the crucible was shown in Figure 6. Without any facilities, the inclusion particles with macro sizes close to 100 μm are mainly distributed in the upper part of the crucible. There exist micro inclusion particles with sizes in the range of 1 μm to 25 μm near the outflow slit nozzle. Adding the stopper, because of the enhanced flow field, the motion of macro inclusion particles in the range of 75 μm to 100 μm speed up. As the porous baffle is equipped, most macro inclusion particles are filtered above the porous zone, and a limited amount of microparticles escape and pass through the porous zone. Furthermore, when the electromagnetic brake is applied, the motion of inclusion particles becomes retarded because of lower melt velocity.

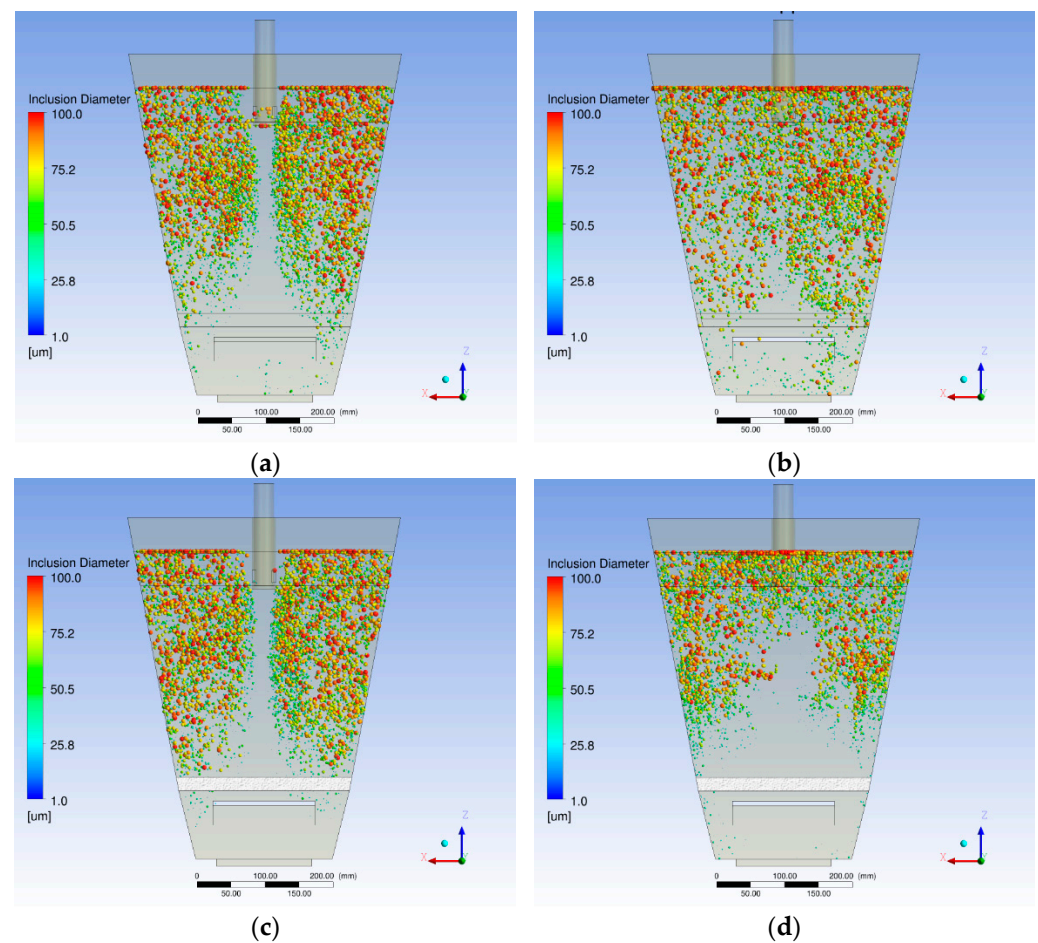


Figure 6. Distribution of inclusion particles predicted by the mathematical modeling using various experimental facilities. (a) Without the facility, (b) with the stopper, (c) with the stopper and porous baffle, (d) with the stopper, porous baffle, and magnetic field.

Consequently, the ratio of particles outflowing through the slit nozzle was statistically analyzed in Figure 7. Compared to the inclusion amount ratios using none of the facilities, when the stopper is used, the ratios of inclusions with the sizes in the various ranges increase, which means that the inclusion removal becomes worse when the stopper is individually used. Subsequently, when the combined application of stopper and the porous baffle is used, the ratios of micro inclusion particles with sizes in the range of 1 μm to 50 μm decrease, but the ratios of macro inclusion particles with sizes in the range of 50 μm to 100 μm increase slightly. When the electromagnetic braking is applied, all ratios of inclusion particles decrease obviously. The amount ratio of macro inclusion particles with sizes ranging from 76 μm to 100 μm dramatically decreases to 0.11%.

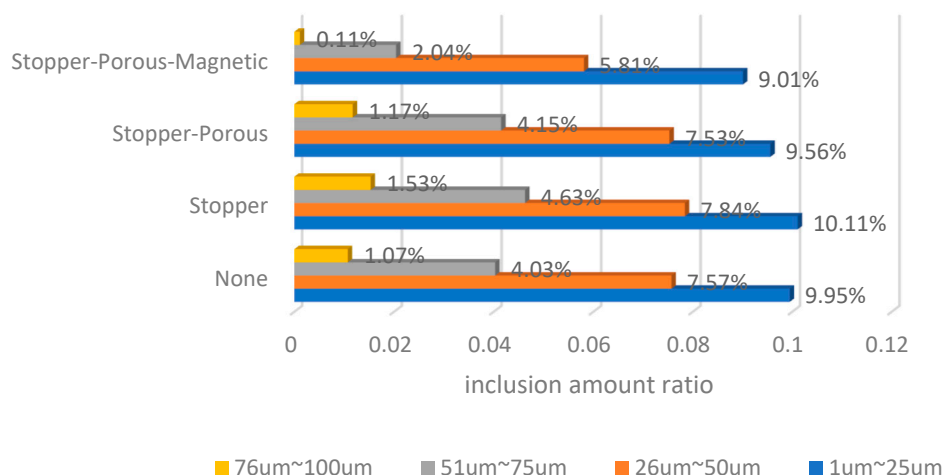


Figure 7. Statistical analysis of the ratio of inclusions particles outflow from the slit nozzle.

4. Conclusions

The flow pattern and inclusion behavior in the crucible during the planar flow casting process were studied. The color dye water experiment was used to show the flow field and validate the mathematical modeling, and the validated mathematical model was employed to predict the inclusion behavior. Several conclusions were drawn as follows:

In terms of the applicability of various turbulence models for simulating flow distribution, the flow pattern predicted by the LES model is maximally consistent with that in the physical modeling in the crucible in PFC process.

Compared to the flow field using none of the facilities, the flow field enhances using the stopper. For the flow pattern using stopper and porous baffle, the flow intensity nearby the submerged nozzle outflow region decreases, and the flow field becomes intense to some extent above the porous zone. Furthermore, as the magnetic field is added, the electromagnetic brake weakens the flow field in the magnetic zone and enhances the flow circulation above the magnetic zone.

In terms of inclusion removal, the inclusion removal worsens when the stopper is individually used compared with that using none of the facilities. When the porous baffle is equipped, the ratio of macro inclusion decreases from 10.11% to 9.56%. The function of the electromagnetic brake to weaken the flow pattern is most efficient for inclusion removal in the crucible in PFC process.

Above all, to produce the broad amorphous ribbon, it is essentially meaningful to propose a novel-designed crucible with various flow-controlling methods for the efficient improvement of the PFC process, homogenization of the temperature, and increasing the ribbon's purity and quality.

Author Contributions: Conceptualization, Y.L. and H.L.; methodology, Y.L. and H.Q.; software, Y.L. and H.Q.; validation, H.Q. and Z.H.; formal analysis, Y.L. and Y.Y.; investigation, Y.L. and H.Q.; resources, H.Q. and Z.H.; data curation, Y.L. and Y.Y.; writing—original draft preparation, Y.L.; writing—review and editing, H.Q.; visualization, Y.L.; supervision, H.L.; project administration, H.L.; funding acquisition, H.L. All authors have read and agreed to the published version of the manuscript.

Funding: This research was funded by National Natural Science Foundation of China, grant number 51774098.

Institutional Review Board Statement: The approval or declaration of this study is not applicable.

Informed Consent Statement: Informed consent of this study is not applicable.

Data Availability Statement: Data sharing of this study is not applicable.

Acknowledgments: The authors gratefully acknowledge the support of the National Natural Science Foundation of China (Grant No. 51774098).

Conflicts of Interest: The authors declare no conflict of interest.

References

1. Lavernia, E.J.; Srivatsan, T.S. The rapid solidification processing of materials: Science, principles, technology, advances, and applications. *J. Mater. Sci.* **2010**, *45*, 287–325. [[CrossRef](#)]
2. Shibuya, K. Production and Magnetic-Properties of Fe-B-Si Amorphous Alloy Ribbons: A Review. *Mater. Sci. Eng. A* **1994**, *181*, 1435–1439. [[CrossRef](#)]
3. Jacobson, L.A.; McKittrick, J. Rapid solidification processing. *Mater. Sci. Eng. R* **1994**, *11*, 355–408. [[CrossRef](#)]
4. Gutierrez, E.M.; Szekely, J. A mathematical model of the planar flow melt spinning process. *Met. Mater. Trans. A* **1986**, *17*, 695–703. [[CrossRef](#)]
5. Takeshita, K.; Shingu, P.H. An Analysis of the Ribbon Formation Process by the Single Roller Rapid Solidification Technique. *Trans. Jpn. Inst. Met.* **1983**, *24*, 529–536. [[CrossRef](#)]
6. Yu, H. A fluid mechanics model of the planar flow melt spinning process under low reynolds number conditions. *Met. Mater. Trans. A* **1987**, *18*, 557–563. [[CrossRef](#)]
7. Geoffroy, O. Soft Nanocrystalline Alloys (Melt Spun). In *New Magnetic Materials and Their Functions” and Workshop on Advanced Magnetic Materials, Cluj-Napoca, Romania, 9–18 September 2007*; STUDIA UNIVERSITATIS: Cluj-Napoca, Romania, 2007; p. 49.
8. Li, B.-S.; Chen, W.-Z.; Zhao, Y.-L.; Zhao, P. Evolution and control of nonmetallic inclusions in FeSiB alloy. *J. Iron Steel Res. Int.* **2020**, *27*, 588–597. [[CrossRef](#)]
9. Zuo, Y.; Wang, S.L.; Huang, Y.; Wang, S.X. Corrosion Resistance of Fe-Based Bulk Amorphous Alloy with Sulfide Inclusion. In *Chinese Materials Conference*; Springer Science and Business Media LLC.: Singapore, 2018; pp. 309–318.
10. Cox, B.L. Planar-Flow Melt Spinning: Process Dynamics and Defect Formation. Ph.D. Thesis, Cornell University, Ithaca, NY, USA, 2011.
11. Su, Y.-G.; Chen, F.; Wu, C.-Y.; Chang, M.-H.; Chung, C.-A. Effects of Manufacturing Parameters in Planar Flow Casting Process on Ribbon Formation and Puddle Evolution of Fe–Si–B Alloy. *ISIJ Int.* **2015**, *55*, 2383–2390. [[CrossRef](#)]
12. Byrne, C.J.; Kueck, A.M.; Baker, S.P.; Steen, P.H. In situ manipulation of cooling rates during planar-flow melt spinning processing. *Mater. Sci. Eng. A* **2007**, *459*, 172–181. [[CrossRef](#)]
13. Kramer, M.; Mecco, H.; Dennis, K.; Vargonova, E.; McCallum, R.; Napolitano, R.E. Rapid solidification and metallic glass formation—Experimental and theoretical limits. *J. Non-Cryst. Solids* **2007**, *353*, 3633–3639. [[CrossRef](#)]
14. Yu, H.; Wang, B.; Li, H.; Li, J. Influence of electromagnetic brake on flow field of liquid steel in the slab continuous casting mold. *J. Mater. Process. Technol.* **2008**, *202*, 179–187.
15. Cho, S.-M.; Thomas, B.G. Electromagnetic Forces in Continuous Casting of Steel Slabs. *Metals* **2019**, *9*, 471. [[CrossRef](#)]
16. Vakhrushev, A.; Kharicha, A.; Liu, Z.; Wu, M.; Ludwig, A.; Nitzl, G.; Tang, Y.; Hackl, G.; Watzinger, J. Electric Current Distribution During Electromagnetic Braking in Continuous Casting. *Met. Mater. Trans. A* **2020**, *51*, 2811–2828. [[CrossRef](#)]
17. Bichi, A.; Smith, W.; Wissink, J. Solidification and downstream meniscus prediction in the planar-flow spin casting process. *Chem. Eng. Sci.* **2008**, *63*, 685–695. [[CrossRef](#)]
18. Bussmann, M.; Mostaghimi, J.; Kirk, D.; Graydon, J. A numerical study of steady flow and temperature fields within a melt spinning puddle. *Int. J. Heat Mass Transf.* **2002**, *45*, 3997–4010. [[CrossRef](#)]
19. Wu, S.; Chen, C.; Hwang, W.; Yang, C. Analysis for melt puddle in the planar flow casting process—A mathematical modelling study. *Appl. Math. Model.* **1992**, *16*, 394–403. [[CrossRef](#)]
20. Chen, C.-W.; Hwang, W.-S. A Modified Free Surface Treatment for the Modeling of Puddle Formation in Planar Flow Casting Process. *ISIJ Int.* **1995**, *35*, 393–401. [[CrossRef](#)]
21. Chen, C.-W.; Hwang, W.-S. A three-dimensional fluid flow model for puddle formation in the single-roll rapid solidification process. *Appl. Math. Model.* **1995**, *19*, 704–712. [[CrossRef](#)]
22. Su, Y.-G.; Chen, F.; Chang, C.-M.; Wu, C.-Y.; Chang, M.-H.; Chung, C.-A. Tuning the Planar-Flow Melt-Spinning Process Subject to Operability Conditions. *JOM* **2014**, *66*, 1277–1286. [[CrossRef](#)]
23. Su, Y.-G.; Chen, F.; Wu, C.-Y.; Chang, M.-H. Simulation for the Effect of Wetting Conditions of Melt Puddle on the Fe–Si–B Ribbon Alloy in the Planar-Flow Melt-Spinning Process. *ISIJ Int.* **2017**, *57*, 100–106. [[CrossRef](#)]
24. Majumdar, B.; Sowjanya, M.; Srinivas, M.; Babu, D.A.; Reddy, T.K.K. Issues on Puddle Formation During Rapid Solidification of Fe–Si–B–Nb–Cu Alloy Using Planar Flow Melt Spinning Process. *Trans. Indian Inst. Met.* **2012**, *65*, 841–847. [[CrossRef](#)]
25. Sowjanya, M.; Reddy, T.K.K. Cooling wheel features and amorphous ribbon formation during planar flow melt spinning process. *J. Mater. Process. Technol.* **2014**, *214*, 1861–1870. [[CrossRef](#)]
26. Liu, H.; Chen, W.; Qiu, S.; Liu, G. Numerical Simulation of Initial Development of Fluid Flow and Heat Transfer in Planar Flow Casting Process. *Met. Mater. Trans. A* **2009**, *40*, 411–429. [[CrossRef](#)]
27. Liu, H.; Chen, W.; Chen, Y.; Liu, G. Thermal Deformation Analysis of the Rotating Roller in Planar Flow Casting Process. *ISIJ Int.* **2010**, *50*, 1431–1440. [[CrossRef](#)]
28. Li, Y.; Yang, Y.; He, C. Three-dimensional transient temperature analysis of cooling roller for preparing amorphous ribbon. *J. Non-Crystalline Solids* **2018**, *481*, 276–281. [[CrossRef](#)]
29. Li, Y.; Yang, Y.; He, C. Temperature and Thermal Expansion Analysis of the Cooling Roller Based on the Variable Heat Flux Boundary Condition. *JOM* **2018**, *70*, 855–860. [[CrossRef](#)]

30. Ansys, I. *Ansys Fluent Theory Guide Version*; RANSYS Inc.: Canonsburg, PA, USA, 2019; pp. 193–195.
31. Chaudhary, R.; Ji, C.; Thomas, B.; Vanka, S.P. Transient Turbulent Flow in a Liquid-Metal Model of Continuous Casting, Including Comparison of Six Different Methods. *Met. Mater. Trans. A* **2011**, *42*, 987–1007. [[CrossRef](#)]
32. Gregorc, J.; Kunavar, A.; Šarler, B. RANS versus Scale Resolved Approach for Modeling Turbulent Flow in Continuous Casting of Steel. *Metals* **2021**, *11*, 1140. [[CrossRef](#)]
33. Li, D.; Lu, Z. The effects of aging on the cyclical thermal shock response of a copper-beryllium alloy as a substrate of cooling wheel in planar flow casting process. *Mater. Res. Express* **2020**, *7*, 116511. [[CrossRef](#)]
34. Andrzejewski, P.; Köhler, K.-U.; Pluschkell, W. Model investigations on the fluid flow in continuous casting moulds of wide dimensions. *Steel Res.* **1992**, *63*, 242–246. [[CrossRef](#)]
35. Jin, X.; Chen, D.; Xie, X.; Shen, J.; Long, M. Investigation on Water Model for Fluid Flow in Slab Continuous Casting Mold with Consideration of Solidified Process. *Steel Res. Int.* **2013**, *84*, 31–39. [[CrossRef](#)]
36. Jin, X.; Chen, D.F.; Zhang, D.J.; Xie, X.; Bi, Y.Y. Water model study on fluid flow in slab continuous casting mould with solidified shell. *Ironmak. Steelmak.* **2011**, *38*, 155–159. [[CrossRef](#)]
37. Zhang, M.; Gu, H.; Huang, A.; Zhu, H.; Deng, C. Physical and mathematical modeling of inclusion removal with gas bottom-blowing in continuous casting tundish. *J. Min. Met. Sect. B Met.* **2011**, *47*, 37–44. [[CrossRef](#)]
38. Liu, Z.; Li, B. Transient motion of inclusion cluster in vertical-bending continuous casting caster considering heat transfer and solidification. *Powder Technol.* **2016**, *287*, 315–329. [[CrossRef](#)]
39. Zhang, K.-T.; Liu, J.-H.; Cui, H. Effect of Flow Field on Surface Slag Entrainment and Inclusion Adsorption in a Continuous Casting Mold. *Steel Res. Int.* **2019**, *91*, 2. [[CrossRef](#)]